Simulation of hard-disk flow in microchannels

Guofei Shen[1,2] and Wei Ge[1,*]

[1]*State Key Laboratory of Multi-phase Complex System, Institute of Process Engineering, Chinese Academy of Sciences, Beijing 100190, China*

[2]*Graduate University of the Chinese Academy of Sciences, Beijing 10049, China*

(Received 3 September 2009; revised manuscript received 30 October 2009; published 5 January 2010)

The dynamic flow behavior of a hard-disk fluid under external force field in two-dimensional microchannels is investigated using an event-driven molecular dynamics simulation method. Simulations have been carried out under laminar and subsonic conditions in both slip regime and transition regime, and the effects of three main factors, Knudsen number (Kn), force field intensity, and packing fraction, on flow and heat transfer behavior have been studied. It is shown that all the factors play important roles in the velocity distribution of the flow, and the temperature profile of the gas flow may exhibit a bimodal shape with a local minimum instead of a maximum in the center. These findings verify the predictions of nonequilibrium kinetic theories on the so-called "temperature dip." At high Kn, the two maxima of temperature shift to two walls and the temperature profile changes to a "parabola" opening upward with a minimum in the center. A slight setback of the temperature is also found before the fluid flow eventually arrives at a steady state when the shear rate is high enough.

DOI: 10.1103/PhysRevE.81.011201 PACS number(s): 47.45.Gx, 83.10.Rs, 05.70.Ln, 47.10.ab

I. INTRODUCTION

Microflow system has recently received great attention for its immense potential applications [1]. However, the fluid behavior at microscale is greatly different from that at macroscale. For gas flow the difference is, in general, related to the Knudsen number (Kn), which is defined as the ratio of the mean-free path of the gas molecules to the characteristic dimension of the flow field. Under high Kn, due to the compressibility and rarefaction effects, velocity slip and temperature jump appear at walls and fluid might show different properties at extremely strong shear rate. Recently, a great deal of researches has been devoted to the flow accelerated by constant force in microchannels. It was found that the temperature profile might exhibit a bimodal shape with a local minimum surrounded by two symmetric maxima, instead of a flat maximum, which was named "temperature dip." It can be predicted from the analytical solution of the kinetic theory [2–12], and has been confirmed qualitatively and semiquantitatively by direct simulation Monte Carlo (DSMC) method [3,13]. Wang *et al.* [14] also observed this phenomenon in simulations using pseudoparticle modeling (PPM) [15,16] when the external force was strong enough. However, duo to technological difficulties, direct observation and measurement of this phenomenon in experiments is still lacking. Molecular dynamics (MD) simulation, based on first principles, can be adopted as a reliable tool to investigate and, to some extent, verify such complicated phenomena and provide information that is not easily obtained by experiments. Especially, the hard sphere (HS) or hard disk (HD) simulation in the event-driven algorithm is a very efficient and exact solution of MD simulation and is most close to experiments for rarefied gases. The hard spheres/disks in this method move from one collision site to the next analytically and the numerical error is only from the rounding of floating point quantities. In this paper, we carry out event-driven hard-disk simulation for the gas flow in microchannels which is driven by a constant external force in the direction parallel to the channel.

II. MODEL AND SIMULATION METHOD

Let us consider the gas flow in a microchannel with a large number of hard disks. As shown in Fig. 1, the width of

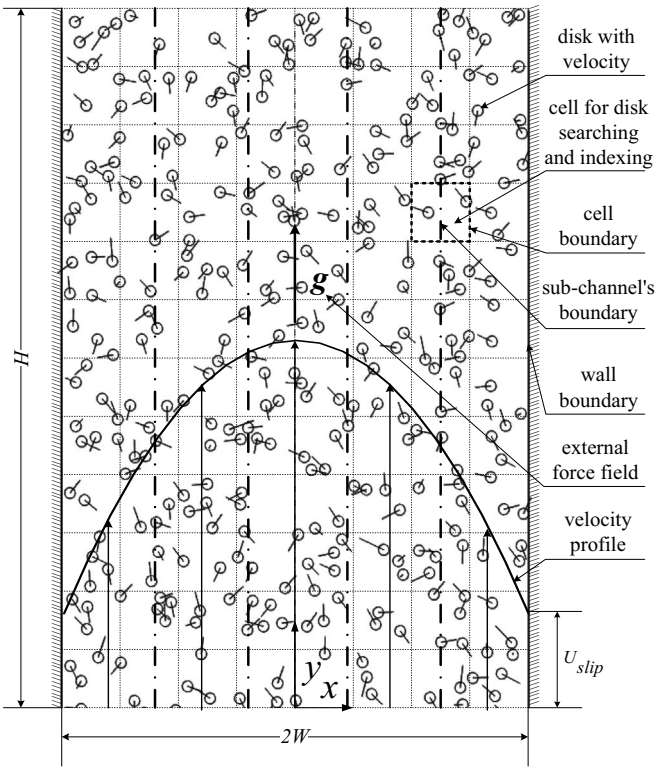

FIG. 1. Schematic of gravity-driven flow composed of hard disks.

*Corresponding author. wge@home.ipe.ac.cn

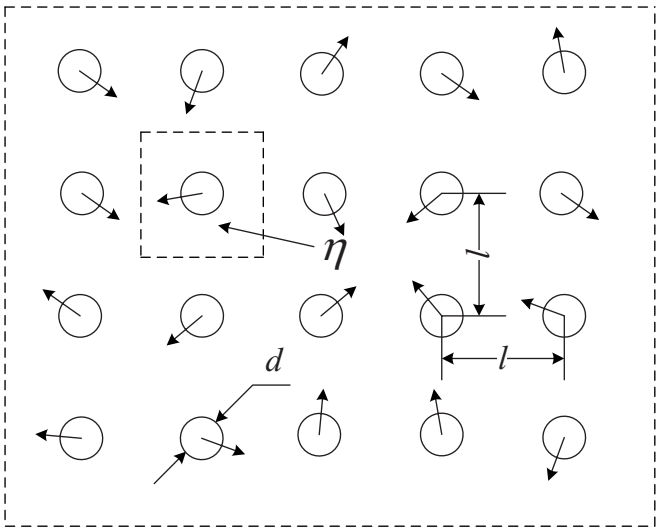

FIG. 2. Schematic of original arrangement of hard-disk system.

the channel is $2W$, while the height is H. The periodic boundary condition is applied in y direction parallel to the channel, so the system is effectively infinite in the flow direction and there are no inlet or outlet effects. Both walls of the channel are maintained at a constant temperature T_w and any gas particle in the domain bears a uniform external force.

For the simulation of the hard disks, the event-driven algorithm is introduced [17–20]. The simulation region is divided into a lattice of small rectangular cells by orthogonal straight lines, and then the disks are assigned to cells on the basis of their positions. These cells are only for searching and indexing purpose, and have no physical effect on the disks. The cell size had better exceed the interaction range of hard disks, i.e., the diameter of the disk. It is not essential for this link-cell structure, but if this condition is not satisfied, disks in further cells also have to be considered for processing the collisions of a disk (schematic drawing of the cells can be seen from the dot lines in Fig. 1). A disk can either collide with another disk or the wall of the channel, or cross the boundaries between the cells. The collisions among disks are assumed to be binary and crossing cell boundary has no physical effect on the motion of the disk. When the collision between two disks happens, linear momentum is conserved and their postcollisional velocities are given as follows:

$$\boldsymbol{v}'_{1,2} = \boldsymbol{v}_{1,2} \mp \frac{(1+e)m_{2,1}}{m_1+m_2}\frac{(\boldsymbol{v}_1-\boldsymbol{v}_2)\cdot(\boldsymbol{P}_1-\boldsymbol{P}_2)}{|\boldsymbol{P}_1-\boldsymbol{P}_2|^2}(\boldsymbol{P}_1-\boldsymbol{P}_2), \tag{1}$$

where subscripts 1 and 2 refer to disks 1 and 2, respectively, m is the mass of the disk, $\boldsymbol{P}$ is the position vector, $\boldsymbol{v}$ is the precollisional velocity, $\boldsymbol{v}'$ is the postcollisional velocity and e is the coefficient of restitution which is taken to be 1.

To reduce the number of influential factors, for particle-wall collisions, the tangential momentum accommodation coefficient is set to 1, i.e., fully diffuse reflection is induced to the wall. If a disk collides with the wall with a given

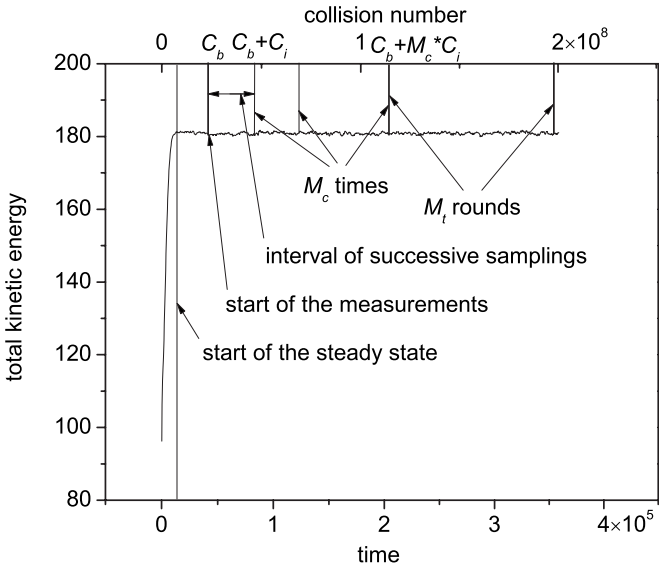

FIG. 3. Schematic of measurements and temporal evolution of the total kinetic energy with $N=240,000$ in hard-disk system at $g=6.0\times10^{-6}$, $\eta=0.0873$ and Kn=0.154.

temperature T_w, its velocity is sampled from the Biased-Maxwell distribution [21],

$$f_\perp(v_x) = \frac{m}{k_B T_w} v_x \exp\left(-\frac{m v_x^2}{2k_B T_w}\right), \tag{2}$$

$$f_\parallel(v_y) = \sqrt{\frac{m}{2\pi k_B T_w}} \exp\left(-\frac{m v_y^2}{2k_B T_w}\right), \tag{3}$$

where k_B is the Boltzmann constant and the subscripts $\perp$ and $\parallel$ denote the normal and tangential components, respectively. According to Box-Muller method, the velocity of the disk is therefore [22],

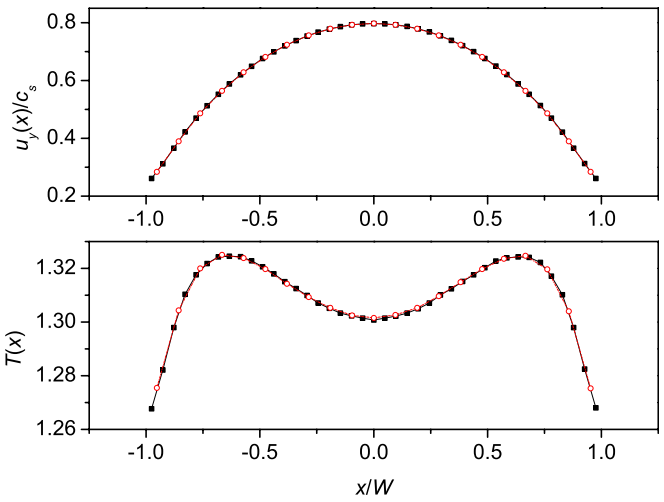

FIG. 4. (Color online) Velocity profiles and temperature profiles with different member of subchannels at $g=6.0\times10^{-6}$, $\eta=0.0873$, and Kn=0.154: continuous line (black with solid square), results with 41 subchannels; dashed line (red with hollow circle), results with 21 subchannels.

TABLE I. Specifications of the simulations for comparison of different subchannels.

Case	W	H	N	M_s	C_b	C_i	M_c	M_t
1	18	240000	240000	21	24000000	200	40000	40
2	18	240000	240000	41	24000000	200	40000	40

$$v_x = \pm \sqrt{-\frac{2k_B T_w}{m}\ln(z_1)}, \tag{4}$$

$$v_y = \sqrt{-\frac{2k_B T_w}{m}\ln(z_2)}\cos(2\pi z_3), \tag{5}$$

where z_1, z_2, and z_3 are random numbers uniformly distributed between 0 and 1, the positive and negative symbols express that the disk's velocity normal to the wall should be reversed after its colliding with the wall.

To characterize the properties of the gas, we recall the compressibility factor of hard-disk system as given by Helfand *et al.* [23] and Verlet and Levesque [24]

$$Z = 1 + 2\chi\eta = (1-\eta)^2, \tag{6}$$

where η is packing fraction. The Enskog factor χ is then derived as

$$\chi = \frac{1-\eta/2}{(1-\eta)^2}. \tag{7}$$

In the simulations, lengths and masses are scaled by the radius (r) and the mass (m) of the disk, respectively. The temperature is scaled by the wall temperature T_w and the Boltzmann constant is $k_B = 2\times10^{-4}$, so the thermal velocity $v_0 = \sqrt{2k_B m/T_w} = 0.02$. The initial temperature of the system T_0 equals T_w. The number of hard disks (N) is 160 000 $\sim$2 000 000 and Kn equals to $\lambda/2W$.

$$\lambda = \frac{\pi d}{8\sqrt{2}\eta\chi}, \tag{8}$$

where λ is the mean free path of the gas molecules and d is the diameter of the disk. According to the definition of Vincenti and Kruger [25]

$$c_s = \sqrt{\gamma\left.\frac{\partial p}{\partial \rho}\right|_T}, \tag{9}$$

the sound speed is then calculated as

$$c_s = v_0\sqrt{\frac{\gamma}{2}[2\eta(1-\eta)^{-3} + (1-\eta)^{-2}]}. \tag{10}$$

where p is the pressure, γ is the specific heat ratio. In our simulations, the c_s is calculated based on the wall temperature T_w. The Mach number $\mathrm{Ma} = v/c_s$, where v is the velocity of the steady fluid in the center, is less than 1 and the Reynolds number (Re) is less than 200, far below the two-dimensional critical Re for transition [26], i.e., the gas flow is, in general, subsonic and laminar.

In our simulations, the hard disks are arranged in arrays of form pitches (l) according to the packing fraction (η) and assigned velocities of equal modules (v_0) in random directions originally (Fig. 2). Each MD run will last for a long time after the flow has reached a steady state and been in equilibrium with the wall temperature (that means the velocity and temperature profiles of the flow will not change any more and the total kinetic energy (E_{total}) of all hard disks reaches a steady value except for weak thermal fluctuations;

$$E_{total} = \frac{m}{2}\sum_{i=1}^{N}(v_{xi}^2 + v_{yi}^2), \tag{11}$$

where v_{xi} and v_{yi} are the x velocity and y velocity of disk i, respectively). The measurements of temperature and velocity start after C_b collisions (including both particle-particle and particle-wall collisions) large enough to ensure that the flow has reached a steady state. The samples are taken at an interval of C_i collisions for M_c times in succession. A new measurement is followed immediately and so on for M_t rounds (Fig. 3). The velocity and temperature profiles of transient states are obtained by taking snapshots of the fluid flow directly at every C_e-th collision from the beginning for M_e times, long after the flow reaches the steady state. On the other hand, to sample large number of disks, large aspect ratio of the channel (H/W) is used.

The flow channel is divided into M_s subchannels (dash-dot lines in Fig. 1) and the local velocity and temperature are obtained by averaging on the velocities and kinetic energies of hard disks which are within the respective subchannels at the times of sampling. The local velocity and temperature of the kth subchannel for the tth measurement are

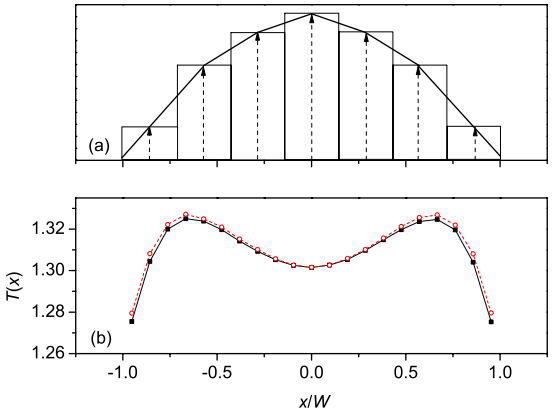

FIG. 5. (Color online) Schematic of the velocity profiles used in different statistical methods (a), and the corresponding simulation results (b): continuous line (black with solid square), results from the method using Eqs. (12)–(16); dashed line (red with hollow circle), results from the method using Eqs. (12) and (15)–(17).

TABLE II. Parameters of the simulation for comparing with the descriptions from Navier-Stokes equations and kinetic theory.

W	H	N	C_b	C_i	M_c	M_t
63	240000	840000	280000000	700	40000	35

$$u_{yt}|_k = \sum_{j=1}^{N_k} v_{yj}/N_k, \tag{12}$$

$$T_t|_k = \frac{m}{2k_B N_k} \sum_{j=1}^{N_k} [(v_{yj} - u_{yt}|_k)^2 + v_{xj}^2], \tag{13}$$

$$N_k = \sum_{i=1}^{M_c} N_{ki}, \tag{14}$$

where v_{xj} and v_{yj} are the velocities of disk j in the kth subchannel, N_{ki} is the number of disks in the kth subchannel at the ith sampling and N_k is the total number of disks in the kth subchannel for M_c times samplings (it should be noted that a disk may present in the same subchannel more than once because the sampling is for M_c times in succession for a measurement). The differences between the results from different rounds of measurements are found to be negligible, demonstrating that the system has indeed reached a steady state. However, to make full use of the measured data and reduce statistical error further, the local velocity and temperature of the kth subchannel are calculated as

$$u_y|_k = \sum_{t=1}^{M_t} u_{yt}|_k/M_t, \tag{15}$$

$$T|_k = \sum_{t=1}^{M_t} T_t|_k/M_t. \tag{16}$$

The value of M_s has an effect on the statistical errors and the velocity and temperature profiles, insufficient subchannels may even cause unwarranted statistical errors. In our simulation, having 21 subchannels is accurate enough for the statistic since the statistical error is only about 0.06% for the velocity and temperature profiles compared with the results from finer profiles with 41 subchannels. The comparison is shown in Fig. 4 and the specifications of the simulations are shown in Table I.

We also obtain the temperature from another statistical method and compare the simulation results with the method mentioned above. The local velocity of the kth subchannel for the tth measurement is computed as Eq. (12) too, but we linearly interpolate the velocity between adjacent subchannels on the average velocity of each subchannel to get a continuous velocity profile $[u_{yt}(x)]$ of the tth measurement. The local temperature of the kth subchannel for the tth measurement is then calculated as

$$T_t|_k = \frac{m}{2k_B N_k} \sum_{j=1}^{N_k} \{[v_{yj} - u_{yt}(x)]^2 + v_{xj}^2\}, \tag{17}$$

different from Eq. (13). Other aspects of this statistical method are the same as the method above. Though this method is more accurate and much more complicated, it is found that the statistical error of the temperature between two statistical methods is only about 0.35%, which validates the adoption of the more simplified method above. The comparison is shown in Fig. 5 and the specifications of the simulation are the same as the case 1 in Table I.

III. RESULTS AND DISCUSSION

The flow under constant external force will reach a steady state after a certain transient stage. If the flow is laminar, the steady velocity and temperature profiles can be derived from

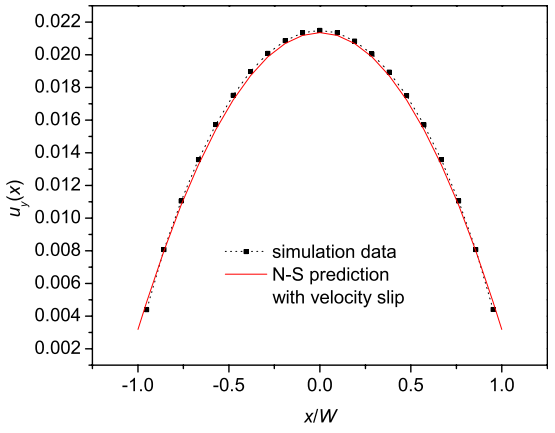

FIG. 6. (Color online) Velocity profile at $g=8.0\times10^{-7}$, $\eta=0.0873$, and Kn=0.044.

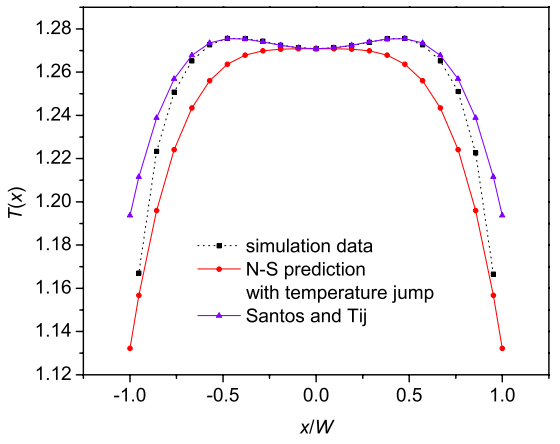

FIG. 7. (Color online) Temperature profile at $g=8.0\times10^{-7}$, $\eta=0.0873$, and Kn=0.044.

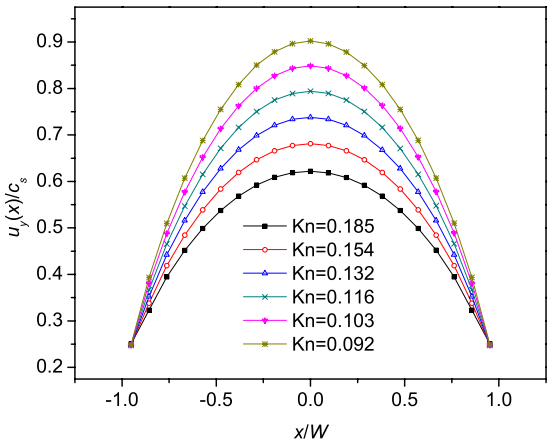

FIG. 8. (Color online) Velocity profiles for different Kn at Fr =0.45 and η=0.0873.

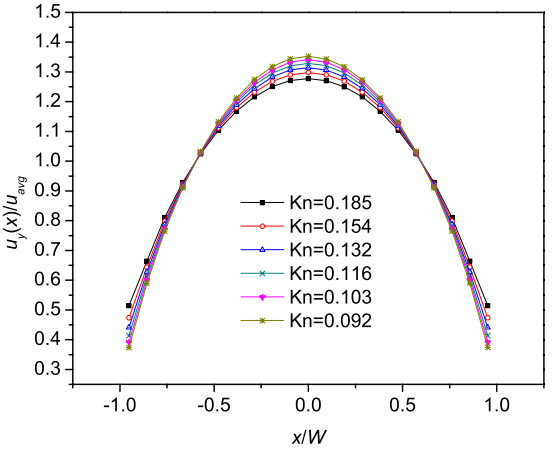

FIG. 9. (Color online) Relative velocity profiles for different Kn at Fr=0.45 and η=0.0873.

the Navier-Stokes equations with velocity slip and temperature jump as follows:

$$u_y(x) = \frac{\rho g W^2}{2\mu}\left[1 - \left(\frac{x}{W}\right)^2\right] + u_{slip}, \tag{18}$$

$$T(x) = \frac{\rho^2 g^2 W^4}{12\kappa\mu}\left[1 - \left(\frac{x}{W}\right)^4\right] + T_w + T_{jump}, \tag{19}$$

where ρ is the mass density, g is the intensity of the external force field, μ and κ are dynamic viscosity and thermal conductivity respectively, u_{slip} and T_{jump} are the velocity slip and temperature jump at the walls, which can be derived from the classical Maxwell-Smoluchowski conditions [1,27]. If thermal creep is not considered, we have

$$u_{slip} = \frac{2-\sigma_v}{\sigma_v}\lambda \left.\frac{\partial u}{\partial y}\right|_w, \tag{20}$$

$$T_{jump} = \frac{2-\sigma_T}{\sigma_T}\frac{2\gamma}{\Pr(\gamma+1)}\lambda \left.\frac{\partial T}{\partial y}\right|_w, \tag{21}$$

where σ_v and σ_T are tangential momentum and energy accommodation coefficients respectively, and Pr is the Prandtl number. In the diffuse reflection case of our simulations, σ_v and σ_T can be both taken as 1. According to Enskog's theory [28], γ=2 and Pr=1/2 for hard-disk system.

This description from the Navier-Stokes equations is compared with our simulation results at η=0.0873 and g=8.0 $\times 10^{-7}$ and the simulation parameters are listed in Table II. As shown in Fig. 6, the simulation data are in good agreement with the prediction of Eq. (18). However, Fig. 7 shows that the temperature profile contradicts the prediction of Eqs. (19) and (21) but agrees well with the description from Santos and Tij [11] in the center using C_T=0.992, which is based on the analyses of the kinetic theory and gives the temperature profile as

$$T(x) = T_M\left[1 - \frac{\rho_M^2 g^2 W^4}{12\mu_M\kappa_M T_M}\left(\frac{x}{W}\right)^4 + C_T\left(\frac{mgW}{k_B T_M}\right)^2\left(\frac{x}{W}\right)^2\right], \tag{22}$$

where the subscripts M denote the midplane, and both the mass density and transport coefficients are assumed to be constant on the cross section. The transport coefficients are all derived from Gass [29]. The dynamic viscosity for a hard-disk gas is

$$\mu = 1.022\frac{1}{2d}\sqrt{\frac{mk_B T}{\pi}}\left[\frac{1}{\chi} + 2\eta + 0.8729(2\eta)^2\chi\right], \tag{23}$$

and thermal conductivity is

TABLE III. Simulation parameters for different Kn at Fr=0.45 and η=0.0873.

Kn	W	H	N	C_b	C_i	M_c	M_t
0.185	15	240000	200000	40000000	200	40000	30
0.154	18	240000	240000	40000000	200	40000	30
0.132	21	240000	280000	40000000	200	40000	30
0.116	24	240000	320000	40000000	200	40000	30
0.103	27	240000	360000	40000000	200	40000	30
0.092	30	240000	400000	40000000	200	40000	30

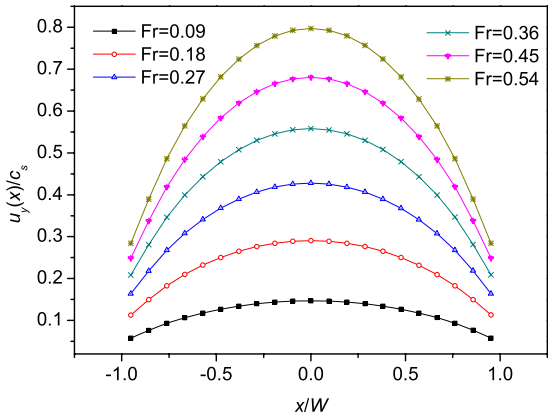

FIG. 10. (Color online) Velocity profiles for different Fr at Kn =0.154 and η=0.0873.

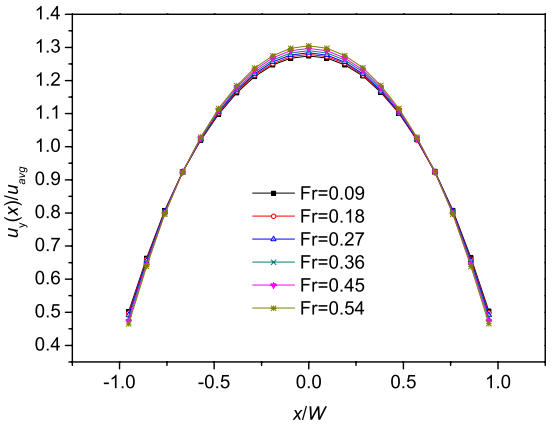

FIG. 11. (Color online) Relative velocity profiles for different Fr at Kn=0.154 and η=0.0873.

$$\kappa = 1.029\frac{2k_B}{d}\sqrt{\frac{k_B T}{\pi m}}\left[\frac{1}{\chi} + 3\eta + 0.8718(2\eta)^2\chi\right], \quad (24)$$

respectively. The discrepancy at the boundaries is considered to be caused by the boundary conditions describing the interaction of the disks with the wall and the fact that Eq. (22) is only applicable to the bulk region of the system sufficiently far from the boundaries [11]. The results of our simulations clearly indicate the shortage of the Navier-Stokes description of the temperature distribution when the gas flow shifts from the slip regime into the transition regime [3]. It should be pointed out that in the two fitting curves the temperature in the mid was taken from the simulation results. However, it can be concluded that our simulations can describe these phenomena at a semiquantitative level and can be used to analyze these phenomena qualitatively. In the following subsections, we will discuss different aspects of the results in detail. To characterize the external force field, the dimensionless number Fr is introduced, which is defined as

$$Fr = \frac{mgW}{k_B T_0}. \quad (25)$$

A. Velocity distributions

Figures 8 and 9 are the velocity profiles and relative velocity profiles at the dimensionless external force intensity of Fr=0.45 and η=0.0873 for different Kn (see Table III for simulation parameters). The relative velocity is defined as the ratio of the velocity to the average velocity of the cross section

$$u_{avg} = \frac{1}{2W}\int_{-W}^{W} u_y(x)dx. \quad (26)$$

In our simulations, it is approximated as

$$u_{avg} = \frac{1}{M_t N M_c}\sum^{M_t}\sum_{i=1}^{NM_c} v_{yi}, \quad (27)$$

where v_{yi} is the y velocity of disk i (It should be noted that a disk may present in the same subchannel more than once because the sampling is for M_c times in succession for a measurement).

Figure 8 shows that lower Kn yields larger velocity at the same Fr and η but the difference of the velocity slip is not obvious. The velocity has a maximum in the center for all Kn and larger relative velocity slip can be easily observed at higher Kn as shown in Fig. 9. In general, the velocity distribution gets much more uniform at higher Kn under the same Fr and η.

Figures 10 and 11 show the velocity profiles and relative velocity profiles for different Fr at Kn=0.154 and η =0.0873 (see Table IV for simulation parameters). With the increase of Fr, the velocity and velocity slip become larger and larger, but the relative velocity distribution does not change basically and always maintains the parabolic form.

Figures 12 and 13 show the effect of packing fraction Kn=0.154 on the velocity profiles and relative velocity pro-

TABLE IV. Simulation parameters for different Fr at Kn=0.154 and η=0.0873.

Fr	W	H	N	C_b	C_i	M_c	M_t
0.09	18	240000	240000	40000000	200	40000	50
0.18	18	240000	240000	40000000	200	40000	50
0.27	18	240000	240000	40000000	200	40000	50
0.36	18	240000	240000	40000000	200	40000	50
0.45	18	240000	240000	40000000	200	40000	50
0.54	18	240000	240000	40000000	200	40000	50

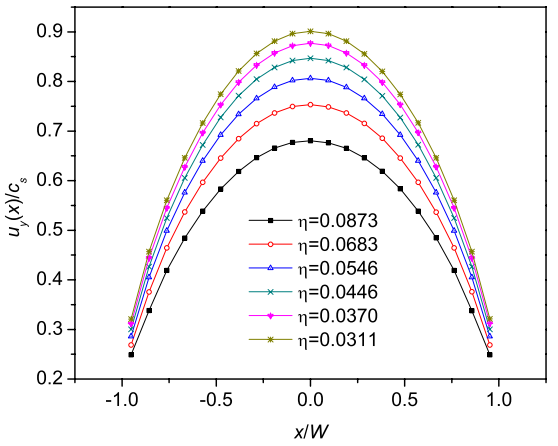

FIG. 12. (Color online) Velocity profiles for different η at Kn =0.154 and Fr=0.45.

files at Kn=0.154 and Fr=0.45 (see Table V for simulation parameters). It is obvious that with the decrease of η, the velocity and velocity slip both get larger but the relative velocity and relative velocity slip are not subject to change and still keep the shape of parabola. All the simulation results above can be fitted by the following correlation:

$$\frac{u_y(x)}{u_{avg}} = \frac{3[1-(x/W)^2]+12\mathrm{Kn}}{2+10\mathrm{Kn}}. \tag{28}$$

It describes the fully developed velocity profile taking into account the effect of Kn.

B. Temperature distributions

Figures 14 and 15 are the temperature profiles and relative temperature profiles for different Kn at Fr=0.45 and η =0.0873 (see Table III for simulation parameters). The relative temperature is defined as the ratio of the temperature to the average temperature of the cross section

$$T_{avg} = \frac{1}{2W}\int_{-W}^{W} T(x)dx, \tag{29}$$

which is approximated in our simulations as

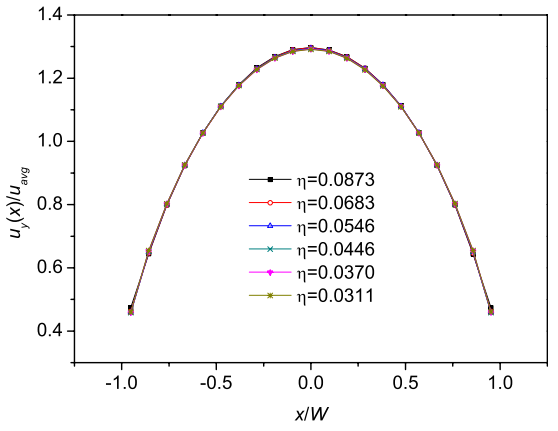

FIG. 13. (Color online) Relative velocity profiles for different η at Kn=0.154 and Fr=0.45.

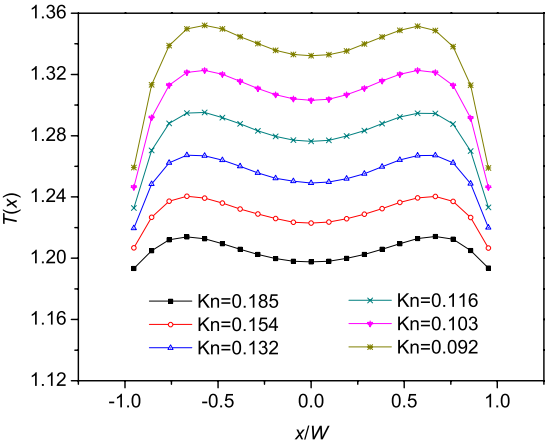

FIG. 14. (Color online) Temperature profiles for different Kn at Fr=0.45 and η=0.0873.

$$T_{avg} = \frac{m}{2k_B M_t N M_c}\sum_{i=1}^{M_t}\sum^{NM_c}[(v_{yi}-u_y|_{(k)})^2+v_{xi}^2], \tag{30}$$

where v_{xi} and v_{yi} are the x velocity and y velocity of disk i, respectively, $u_y|_{(k)}$ is the average velocity of the kth subchannel in which disk i exists (it should be noted that a disk may present in the same subchannel more than once because the sampling is for M_c times in succession for a measurement). It can be observed that the temperature jump becomes larger as Kn decreases at the same Fr and η while relative temperature jump becomes smaller. In Figs. 14 and 15, it shows clearly that the temperature has a local minimum instead of a flat maximum in the middle layer. This behavior agrees with the solution of Eq. (22) as discussed before. The two figures reveal that as Kn decreases under the same Fr and η, the difference between the temperature maxima and minimum in the center becomes larger and the positions of the temperature maxima are moving closer to the center from both sides.

Observed in Fig. 16(a), it is rather surprising that when Kn is large enough, the bimodal shape disappears and the positions of temperature maxima are almost at the walls, overlapping with the temperature jump. In fact, the tempera-

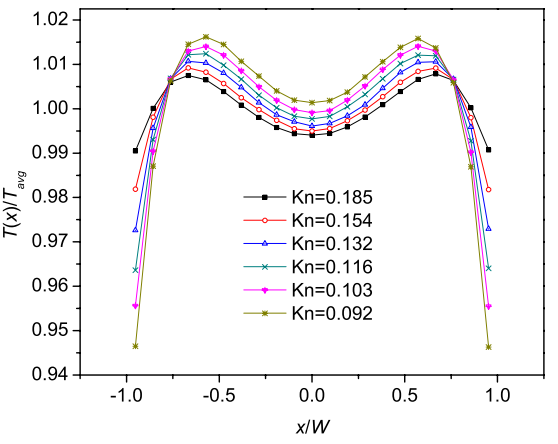

FIG. 15. (Color online) Relative temperature profiles for different Kn at Fr=0.45 and η=0.0873.

TABLE V. Simulation parameters for different η at Kn=0.154 and Fr=0.45.

η	W	H	N	C_b	C_i	M_c	M_t
0.0873	18.00	240000.00	240000	40000000	200	40000	45
0.0683	23.74	271363.76	280000	48000000	200	40000	44
0.0546	30.34	303368.00	320000	56000000	200	40000	43
0.0446	37.79	335871.60	360000	64000000	200	40000	42
0.0370	46.09	368755.65	400000	72000000	200	40000	41
0.0311	55.27	401940.80	440000	80000000	200	40000	40

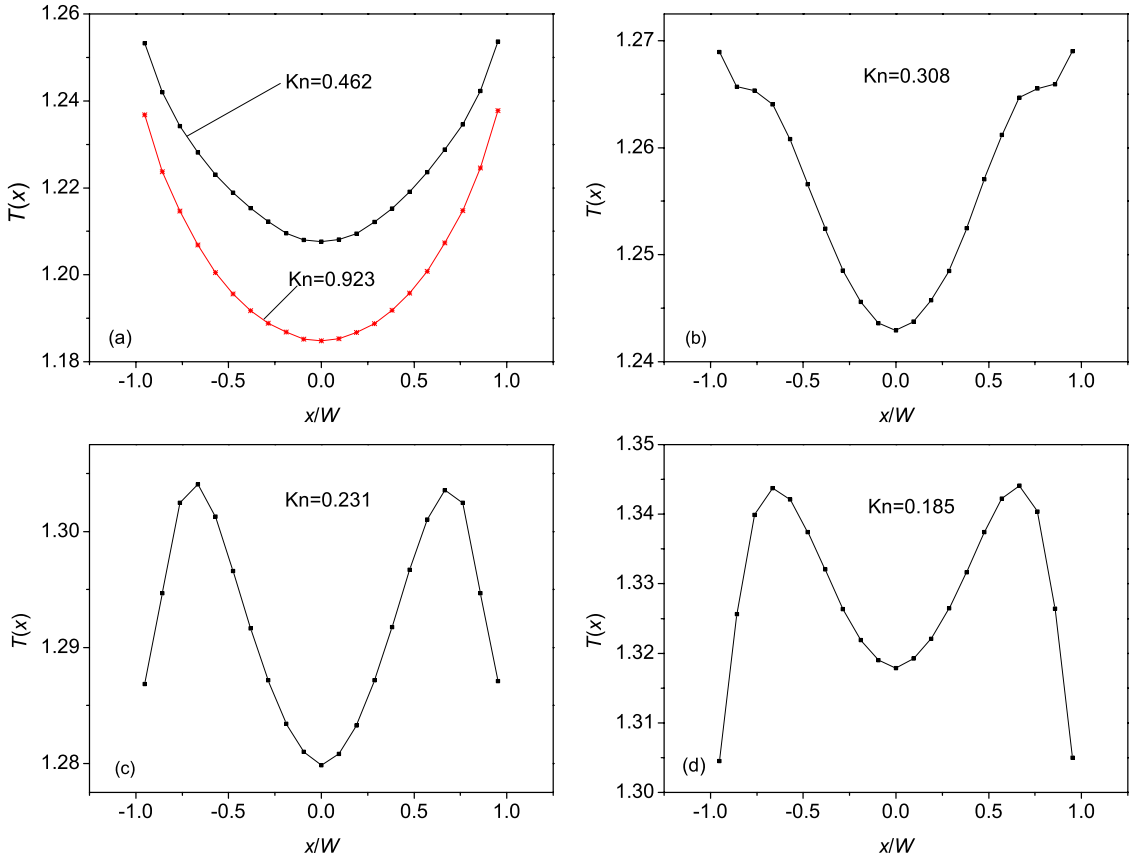

FIG. 16. (Color online) The development of temperature profile with the decrease of Kn at Fr=0.60 and η=0.0873.

TABLE VI. Simulation parameters for decreasing Kn at Fr=0.60 and η=0.0873.

Kn	W	H	N	C_b	C_i	M_c	M_t
0.923	3	12000000	2000000	180000000	900	40000	35
0.462	6	1200000	400000	20000000	100	40000	55
0.308	9	900000	450000	20000000	100	40000	55
0.231	12	240000	160000	40000000	200	40000	55
0.185	15	240000	200000	40000000	200	40000	35

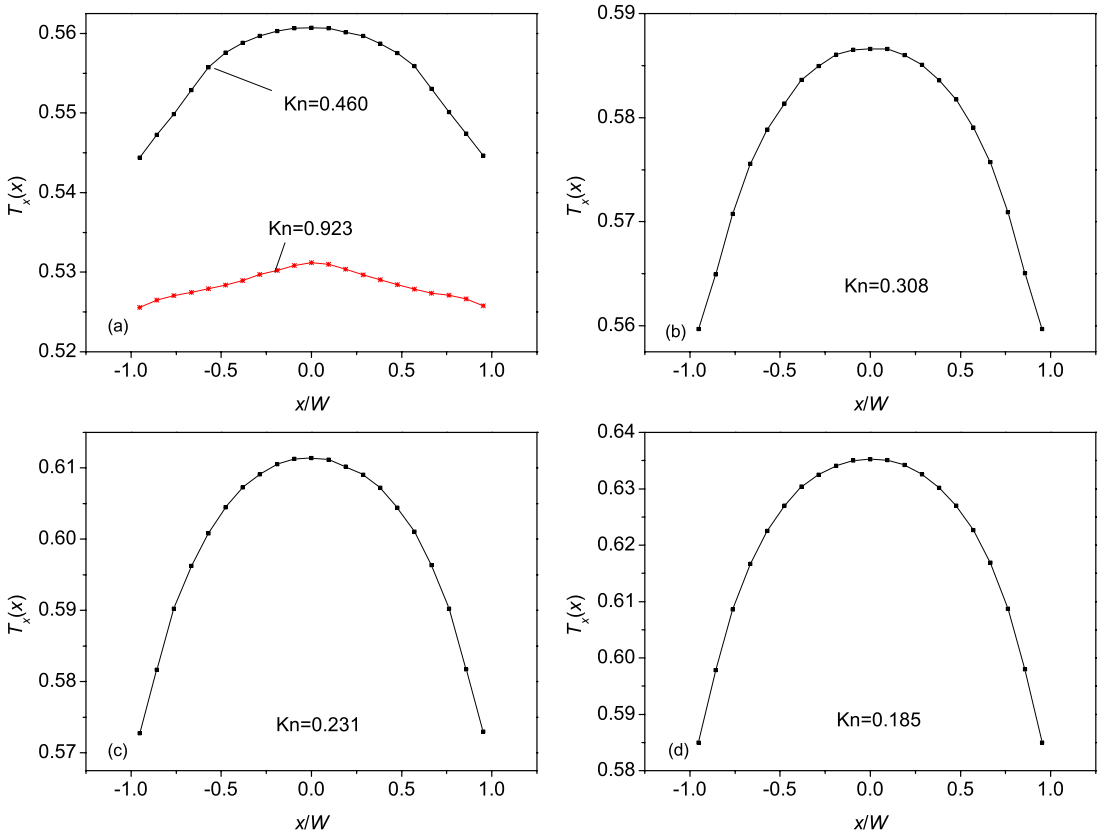

FIG. 17. (Color online) $T_x(x)$ with the decrease of Kn at Fr=0.60 and η=0.0873.

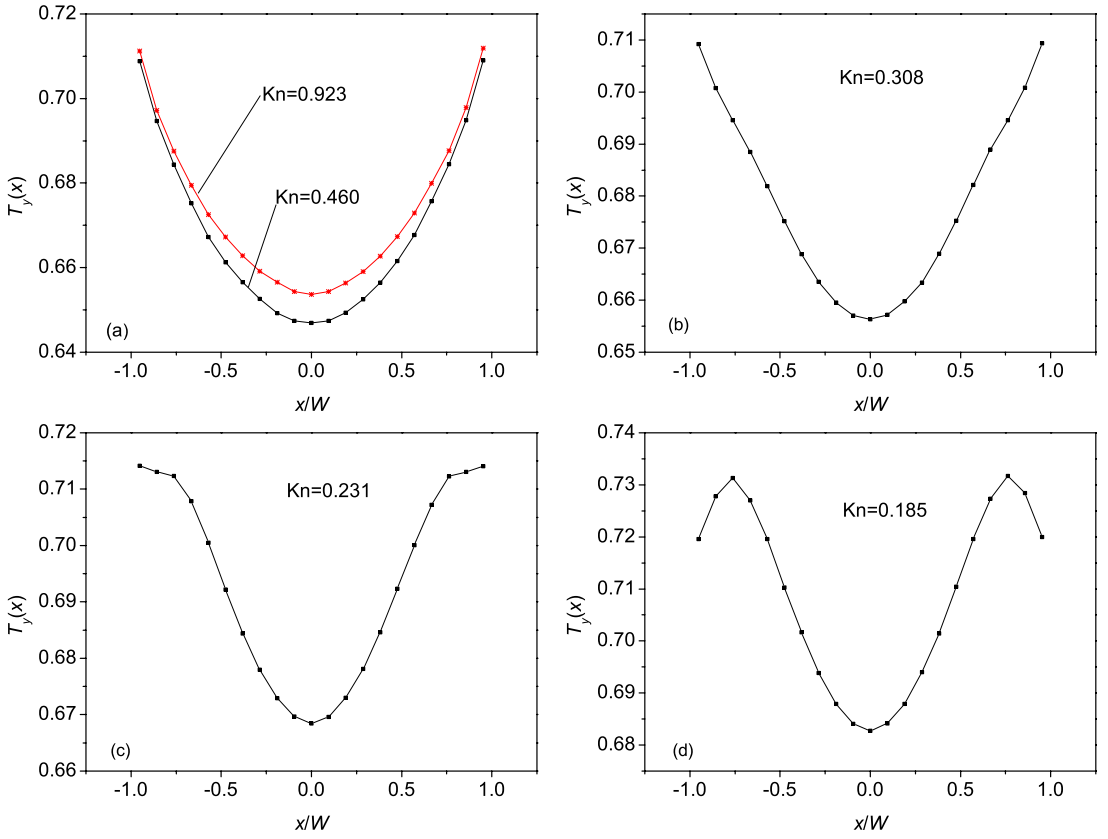

FIG. 18. (Color online) $T_y(x)$ with the decrease of Kn at Fr=0.60 and η=0.0873.

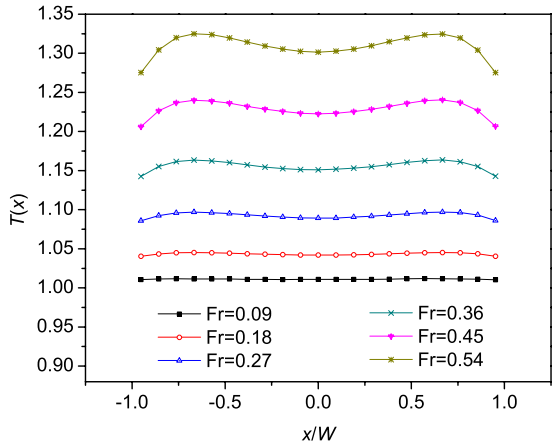

FIG. 19. (Color online) Temperature profiles for different Fr at Kn=0.154 and η=0.0873.

ture curve becomes a "parabola" opening upward. Further study in Fig. 16 shows that, with the reduction of Kn under the same Fr and η, the temperature curve reshapes gradually. At first, the curve has two inflexion points near the walls but the maxima are still at two walls and the minimum is in the center [Fig. 16(b)]. Then, as expected, the two inflexion points become two stationary points with temperature maxima, but the minimum is still in the center [Fig. 16(c)]. As Kn decreases further, the temperature in the center becomes higher than those at the walls finally [Fig. 16(d)], as discussed previously. The simulation parameters are listed in Table VI.

If we define the radial (x) and axial (y) components of the temperature of the kth subchannel for the tth measurement as

$$T_{xt}|_k = \frac{m}{2k_B N_k} \sum_{j=1}^{N_k} v_{xj}^2, \tag{31}$$

$$T_{yt}|_k = \frac{m}{2k_B N_k} \sum_{j=1}^{N_k} (v_{yj} - u_y|_k)^2, \tag{32}$$

respectively, we have the temperature of the kth subchannel for the tth measurement

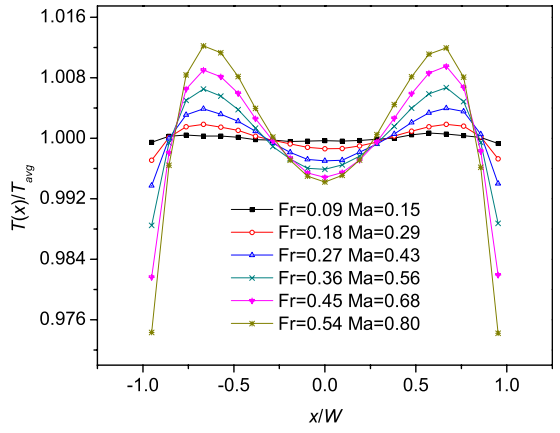

FIG. 20. (Color online) Relative temperature profiles for different Fr at Kn=0.154 and η=0.0873.

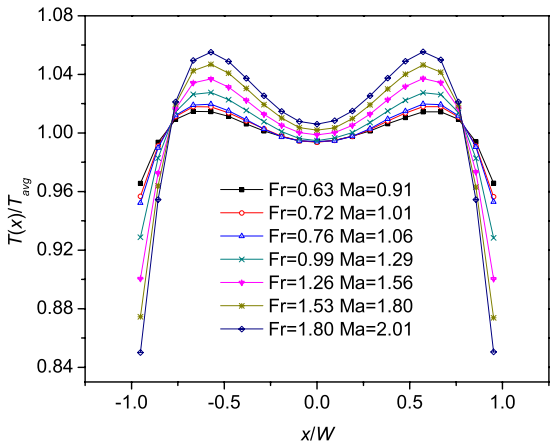

FIG. 21. (Color online) Relative temperature profiles for high Fr values at Kn=0.154 and η=0.0873.

$$T_t|_k = T_{xt}|_k + T_{yt}|_k, \tag{33}$$

and their averages

$$T|_k = T_x|_k + T_y|_k. \tag{34}$$

Figures 17 and 18 present the anisotropy of the two components clearly. $T_x(x)$ has a maximum in the center and gets flatter and flatter with the decrease of Kn, which is in accordance with the Navier-Stokes prediction. But $T_y(x)$ shows a totally different phenomenon. The maximum of $T_y(x)$ first appears at two walls and then moves closer to the center. It clearly reveals that the positions of the minima and the deviation of the temperature profiles from the Navier-Stokes description are mainly caused by the axial temperature component.

Figures 19 and 20 show the temperature profiles and relative temperature profiles for different Fr values at Kn =0.1531 and η=0.0873 (see Table IV for simulation parameters). With the increase of Fr, the temperature in the center increases. In addition, the bimodal shape of temperature profile gets more and more visible and the difference between the two maxima and the slight minimum in the center be-

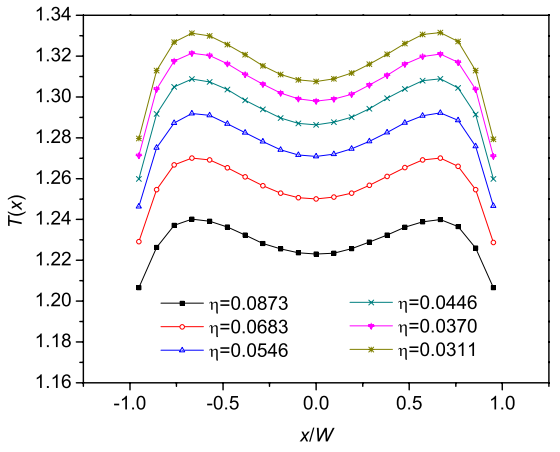

FIG. 22. (Color online) Temperature profiles for different η at Kn=0.154 and Fr=0.45.

TABLE VII. Simulation parameters for high Fr values at Kn=0.154 and η=0.0873.

Fr	W	H	N	C_b	C_i	M_c	M_t
0.63	18	240000	240000	64000000	200	40000	32
0.72	18	240000	240000	64000000	200	40000	32
0.76	18	240000	240000	64000000	200	40000	32
0.99	18	240000	240000	64000000	200	40000	32
1.26	18	240000	240000	64000000	200	40000	32
1.53	18	240000	240000	64000000	200	40000	32
1.80	18	240000	240000	64000000	200	40000	32

comes larger and larger. Moreover, the temperature jump becomes larger but the relative temperature jump becomes smaller. It is interesting that as Ma in the center increases across about 1 (see Figs. 20 and 21, where Re maximum is about 23 and the flow is of course laminar), the relative temperature in the center decreases at first and then increases (The specifications of Fig. 21 are listed in Table VII).

The effects of packing fraction η on temperature and relative temperature, for fixed values of Kn and Fr, are illustrated in Figs. 22 and 23 (see Table V for simulation parameters). The main finding is that, with the decrease of η, both the temperature and the temperature jump increase gradually. But all the temperature profiles maintain a minimum in the center surrounded by two maxima. There are only small differences between the relative temperature profiles except for a slight decrease of the relative temperature jump with the decrease of η.

Finally, the development of temperature profile is shown in Fig. 24 (where the Ma is 3.24 and the Re is about 94, so the flow is still laminar. It should be noted that 3.24 is scaled by the wall temperature T_w. If it is scaled by the temperature in the center of the steady fluid, Ma is about 1.55. The parameters of simulations are listed in Table VIII). The temperature near both walls increases more quickly, as compared with the center. It can also be observed that when Ma$>$1, there is slight setback of the temperature before it arrives at the steady state, which narrows the difference between the maxima and the central minimum. The reason for this setback is still under investigation.

IV. CONCLUSIONS

In this paper, event-driven hard-disk simulation of the gas flow in microchannels is carried out. It is found that our simulation can describe the "temperature dip" phenomenon which verifies the analyses of the kinetic theory and can provide valuable information for experiments in the future. The results show that velocity and velocity slip of the gas flow both increase as the external force intensity increases under the same Kn and η. The fluid velocity becomes larger with the decrease of Kn at the same Fr and η, and η does not affect the distribution of the relative velocity basically. Kn plays a significant role in fluid temperature distribution. When Kn is large enough, the temperature profile is a "parabola" opening upward, and the temperature maxima are at the walls, while the minimum is in the center. With the decrease of Kn, the temperature curve displays two inflection points which then evolves into two stationary points. Thereafter, the temperature in the center increases gradually and becomes higher than those at the walls, but the temperature dip remains. The temperature distribution returns to the normal form when Kn is sufficiently small. These findings are in good agreement with the prediction of nonequilibrium kinetic theory. A slight setback of the temperature profile in the evolution before it approaches the steady state is also observed. To elucidate the mechanism behind these highly nonequilibrium phenomena, more accurate simulations on three-dimensional system of equivalent size is needed and is now underway.

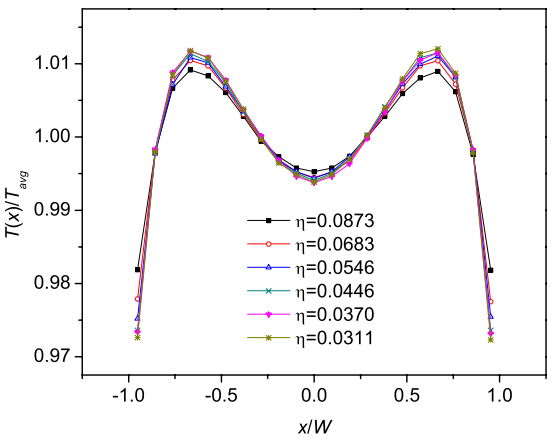

FIG. 23. (Color online) Relative temperature profiles for different η at Kn=0.154 and Fr=0.45.

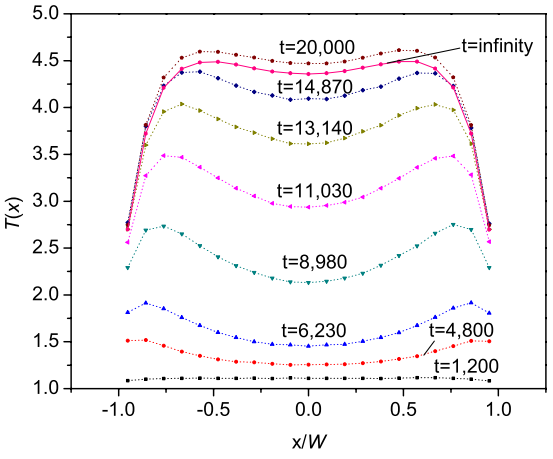

FIG. 24. (Color online) Temporal evolution of the temperature profile at Kn=0.0616, Fr=2.025 and η=0.0873.

TABLE VIII. Parameters of the simulation for temporal evolution of the temperature profile at Kn=0.0616, Fr=2.025, and η =0.0873. The abbreviations are mentioned in second section.

W	H	N	C_b	M_e
45	600000	1500000	200000	1000

ACKNOWLEDGMENTS

This work is financially supported by the National Natural Science Foundation of China under Grant No. 20221603, by the Ministry of Science and Technology of China under Grant No. 2008BAF33B01 and by Chinese Academy of Sciences under Grants No. ZDYZ2008-2 and KGCX2-YW-124.

[1] G. Karniadakis and A. Beskok, *Microflows and Nanoflows: Fundamentals and Simulation* (Springer, New York, 2005).
[2] M. Tij and A. Santos, J. Stat. Phys. **76**, 1399 (1994).
[3] M. Malek Mansour, F. Baras, and A. L. Garcia, Physica A **240**, 255 (1997).
[4] D. Risso and P. Cordero, Phys. Rev. E **58**, 546 (1998).
[5] M. Tij, M. Sabbane, and A. Santos, Phys. Fluids **10**, 1021 (1998).
[6] S. Hess and M. Malek Mansour, Physica A **272**, 481 (1999).
[7] K. Aoki, S. Takata, and T. Nakanishi, Phys. Rev. E **65**, 026315 (2002).
[8] K. Xu, Phys. Fluids **15**, 2077 (2003).
[9] M. Tij and A. Santos, J. Stat. Phys. **117**, 901 (2004).
[10] K. Xu and Z. H. Li, J. Fluid Mech. **513**, 87 (2004).
[11] A. Santos and M. Tij, in *Modelling and Numerics of Kinetic Dissipative Systems*, edited by L. Pareschi, G. Russo, and G. Toscani (Nova Science Publishers, New York, 2006), Chap. 5.
[12] H. Struchtrup and M. Torrilhon, Phys. Rev. E **78**, 046301 (2008).
[13] Y. H. Zheng, A. L. Garcia, and B. J. Alder, J. Stat. Phys. **109**, 495 (2002).
[14] L. Wang, W. Ge, and F. Chen, Chin. Sci. Bull. **52**, 450 (2007).
[15] W. Ge and J. H. Li, *in Proceedings of the Fifth International Conference on Circulating Fluidized Beds*, edited by J. H. Li and M. Kwauk (Science Press, Beijing, 1996), p. 260.
[16] W. Ge and J. Li, Chem. Eng. Sci. **58**, 1565 (2003).
[17] B. J. Alder and T. E. Wainwright, J. Chem. Phys. **27**, 1208 (1957).
[18] B. J. Alder and T. E. Wainwright, J. Chem. Phys. **31**, 459 (1959).
[19] D. C. Rapaport, J. Comput. Phys. **34**, 184 (1980).
[20] M. Marín, D. Risso, and P. Cordero, J. Comput. Phys. **109**, 306 (1993).
[21] G. A. Bird, *Molecular Gas Dynamics and the Direct Simulation of Gas Flows* (Clarendon, Oxford, 1994).
[22] G. Shen, L. Wang, W. Ge, and X. Li, Comput. Appl. Chem. **26**, 539 (2009) (in Chinese with English abstract).
[23] E. Helfand, H. L. Frisch, and J. L. Lebowitz, J. Chem. Phys. **34**, 1037 (1961).
[24] L. Verlet and D. Levesque, Mol. Phys. **46**, 969 (1982).
[25] W. G. Vincenti and C. H. Kruger, *Introduction to Physical Gas Dynamics* (Wiley, New York, 1965).
[26] S. A. Orszag and L. C. Kells, J. Fluid Mech. **96**, 159 (1980).
[27] E. H. Kennard, *Kinetic Theory of Gases* (McGraw-Hill, New York, 1938).
[28] S. Chapman and T. G. Cowling, *The Mathematical Theory of Non-uniform Gases* (Cambridge University Press, Cambridge, England, 1970).
[29] D. Gass, J. Chem. Phys. **54**, 1898 (1971).